IEEE Access
Multidisciplinary | Rapid Review | Open Access Journal

Received December 4, 2020, accepted December 16, 2020, date of publication December 25, 2020, date of current version January 7, 2021.

Digital Object Identifier 10.1109/ACCESS.2020.3047509

Milled Microchannel-Assisted Open D-Channel Photonic Crystal Fiber Plasmonic Biosensor

M. HUSSAYEEN KHAN ANIK[1], M. IFAZ AHMAD ISTI[1], S. M. RIAZUL ISLAM[2], (Member, IEEE), SAKIB MAHMUD[1], HRITESHWAR TALUKDER[1], (Member, IEEE), MD. JALIL PIRAN[2], (Member, IEEE), SHOVASIS KUMAR BISWAS[3], (Member, IEEE), AND KYUNG-SUP KWAK[4], (Life Senior, IEEE)

[1]Department of Electrical and Electronic Engineering, Shahjalal University of Science and Technology, Sylhet 3114, Bangladesh
[2]Department of Computer Science and Engineering, Sejong University, Seoul 05006, South Korea
[3]Department of Electrical and Electronic Engineering, Independent University, Bangladesh (IUB), Dhaka 1229, Bangladesh
[4]School of Information and Communication Engineering, Inha University, Incheon 22212, South Korea

Corresponding authors: Shovasis Kumar Biswas (biswassk@iub.edu.bd) and Kyung-Sup Kwak (kskwak@inha.ac.kr)

(M. Hussayeen Khan Anik, M. Ifaz Ahmad Isti, and S. M. Riazul Islam are co-first authors.)

This work was supported by the National Research Foundation of Korea-Grant funded by the Korean Government (Ministry of Science) under Grant ICT-NRF-2020R1A2B5B02002478.

ABSTRACT A surface plasmon resonance (SPR) based photonic crystal fiber (PCF) sensor having a milled microchannel, and an open D-channel has been proposed in this paper. The sensor shows good functionality in the wide sensing range of 1.14-1.36 Refractive Index Units (RIU) of the analyte, having the capability to detect low refractive index (RI). The Finite Element Method (FEM) based numerical investigations dictate that the proposed sensor has been able to gain a maximum wavelength sensitivity of 53,800 nm/RIU according to the wavelength interrogation technique. The amplitude interrogations show that the sensor has the highest amplitude sensitivity of 328 RIU^{-1}. The highest FOM (Figure of Merit) has been found to be 105 RIU^{-1}. The sensor evinces a minimum wavelength resolution of 1.86×10^{-6} RIU, which secures high detection accuracy. A circular perfectly matched layer (PML) is implemented in the sensor's outermost layer as a boundary condition to absorb surface radiations. Gold is the plasmonic metal, while TiO_2 acts as the adhesive layer for gold attachment on silica. Due to the high sensitivity with a broad range of analyte detection, the sensor is well suited for practical biochemical detection purposes.

INDEX TERMS Broad sensing range, low analyte refractive index, plasmonic oscillations, wavelength sensitivity.

I. INTRODUCTION

A photon coupling to an exciton gives rise to a polariton at the right frequency. The plasmonic oscillations occurring on a metal surface produce surface plasmonic waves (SPW). SPWs can occur in a metal-dielectric interface when photons with the right energy are absorbed under resonance conditions. This optical phenomenon has been engineered to act like a biosensor for biochemical analyte detection purposes. The SPR technology has shown good promise as a new optically advanced sensing scheme for its dynamic applications. These applications include temperature sensing [1], chemical sensing [2], label-free applications [3], and many more. With the advancement of the fabrication technology, porous silica formation has been employed for sensing purposes [4]. SPR based PCF has found its way to widespread applications in biological implications. It has been reported that cancer cell detection is possible with this SPR based PCF biosensor [5]. Early detection of blood cancer is also reported in [6]. Recently, it has been reported that using plasmonic photothermal effect (PPT) in combination with localized SPR (LSPR), the genetic and nucleic acid testing of the coronavirus is possible [7]. It indicates Covid19 detection with more precision than the routinely utilized RT-PCR (Reverse Transcription Polymerase Chain Reaction) technique. The LSPR peak shifts have been reported to be utilized previously to detect the neurotoxin, ADDL (Amyloid β-derived diffusion ligand) related to Alzheimer's disease [8]. Refractive index detection of low carbon alcohols, such as methanol, ethanol, butanol, propanol, and phenol is possible

The associate editor coordinating the review of this manuscript and approving it for publication was Norbert Herencsar.

using PCF SPR sensors [9]. In this work, the specific alcoholic analytes that are mentioned here are sensed based on SPR such that, the analytes are detected solely based on their refractive index. The highest wavelength sensitivity of the lattice design is 40,000 nm/RIU. However, the transmittance profile depicts that, there has been multiple resonance in the same wavelength for the same analyte, which puts forward a detection hindrance.

Plasmonic metals like gold and silver are most commonly used in designing biosensors with the SPR technology, because of the inter-band transitions as the metals are the noble ones. Gold is more preferred due to its higher chemical stability and higher resonance wavelength peak shifts. One of the most sensitive photonic crystal designs with only circular arrangements has been proposed in [10], where the highest wavelength sensitivity, S_λ is 28,000nm/RIU and the maximum amplitude sensitivity S_A is 6829 RIU^{-1}. The RI sensing range of the analyte lies in 1.33-1.42 RI. However, with the advancement of the fabrication technology, different D-shaped open channel PCF-SPR sensors have been designed, which show higher sensitivity with a broad analyte sensing range. A novel D-shape design has been proposed that shows the highest $S_\lambda = 11055$ nm/RIU within 1.20-1.29 RI of analytes [11]. Another team of researchers modified the airhole orientation of the design in recent years to gain a maximum $S\lambda = 20{,}000$nm/R.I.U [12]. in the broad analyte sensing range 1.18-1.36 RI, capable of detecting low RI of analytes. However, their sensitivities are moderate in comparison to the most recent advancements in PCF SPR sensor designs. For accelerating the enhancement of the analyte's coupling more with the incident light wave guided through the core region, dual D-shape open-channel designs have also been proposed [13]. However, the wavelength sensitivity is quite low in the analyte sensing range 1.33-1.39 RI. Several dual D-shape open channels have been modeled, but the sensitivity did not reach moderately high values with respect to the different sensing ranges [14]–[16]. A circularly slotted multiple D-channel design has been proposed, which shows the highest $S_\lambda = 16{,}000$nm/RIU in the sensing range 1.40-1.46 RI [17]. Though the D-shape designs have introduced more volume of the analyte to interact with the core, the photonic crystal orientation did not support the lattice design to reach moderately high sensitivity values. All these lattice designs have been modeled, and the numerical explorations have been conducted using the FEM. Very few works have been conducted previously, which show good sensitivity with analyte RI changes. Similar work with a sensor design has been proposed and fabricated with moderate sensitivity [18].

The PCF sensor design introduced in this work utilizes an open D-channel along with a U-shaped deep groove channel to form the lattice design. Airhole arrangements have been carefully designed such that the periodic variations of the refractive index of airholes result in good coupling. Gold is the plasmonic metal with TiO_2 as the adhesive layer, which attaches gold with silica and enhances the evanescent field's effect on the surface plasmons. The sensor has a broad refractive index sensing range of analytes ranging from 1.14-1.36 RI, capable of detecting lower refractive index analytes. Any type of optically isotropic liquid analyte with refractive index within our detectable sensing range 1.14-1.36 RI is possible to be detected and sensed with our lattice design structure with high sensitivity. The highest wavelength sensitivity has been ascertained to be 53,800 nm/RIU, with the highest $S_A = 328$ RIU^{-1}. This is the highest spectral sensitivity that has been achieved in this broad analyte sensing range to the best of our knowledge, capable of detecting very low refractive indices of analytes.

II. THEORETICAL CONSIDERATIONS

As mentioned earlier, a photon coupling to an exciton produces a polariton, which is a part-light part-matter quasi-particle. This light-matter interactive optical phenomenon is responsible for the optical energy to be absorbed to create electronic oscillations in a metal. The metallic nanoparticles act as the quantum well, where the photon energy is utilized to create an electron-hole pair, which again gives up its energy to convert back to photons. In the presence of a metal-dielectric interface, when an electromagnetic wave falls on it, maximum optical energy is transferred from the incoming light to the surface electronic oscillations on the metal, known as surface plasmons at resonance condition. SPR can be achieved with the right wavelength of the electromagnetic (EM) wave entering the rightly suited crystal orientation of the PCF waveguide. SPWs give rise to the electric field generated at the interface. SPWs travel forward along with the interface. This corresponds to propagation constant [19]

$$\beta = \frac{\omega}{c}\sqrt{\frac{\epsilon_M \epsilon_D}{\epsilon_M + \epsilon_D}} \tag{1}$$

Here, ω is the angular frequency, c is the velocity of light. The metal and the dielectric medium have permittivity ϵ_M and ϵ_D.

The phases coincide when the propagation constants of the incident light wave and the SPWs coincide. This leads to the matching of the frequency and the momentum of both the waves. Maximum modal power is delivered at this resonance condition. This causes the propagation loss to get elevated at resonant wavelengths due to the leaky gaussian nature of the core mode under such conditions. This confinement loss has a linear relation with effective mode index imaginary part $\mathrm{Im}(n_{eff})$ [10]

$$CL = 8.686 \times k_0 \times Im\left(n_{eff}\right) \times 10^4 \ (dB/cm) \tag{2}$$

where, $k_0 = \frac{2\pi}{\lambda}$ is the wave number in the free area.

III. MODELLING AND NUMERICAL ANALYSIS

The representational model of the sensor is illustrated in Figure 1(a). The combination of a D-shape channel and a milled deep groove microchannel placed at the top and bottom of the sensor forms up the sensor design. Airholes have been arranged with four different diameters marked as da_1, da_2, da_3, and da_4 with a square lattice around the center

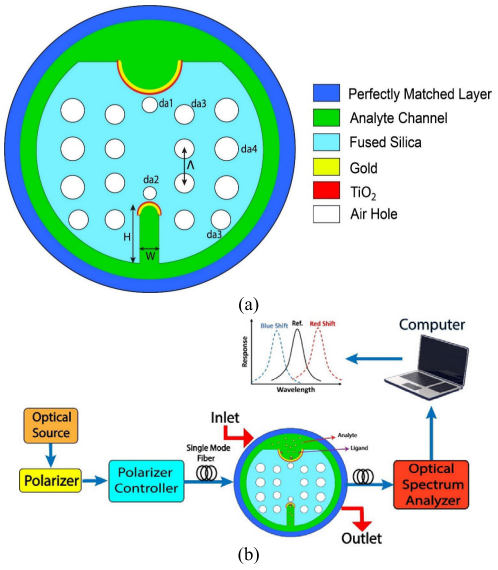

FIGURE 1. (a) Geometry and (b) experimental setup for making the sensor functional.

of the sensor. For better internment of the electric field in the core, air holes have been placed incrementally from inwards to outwards. Two different airholes with diameters of da_1 and da_2 are placed separately just under the D shape channel and above the U-shaped deep groove, respectively. These airholes assist in creating a stable core mode with respect to λ alterations of the incoming EM wave. The D-channel and the groove's apex are coated with gold, which is the plasmonic metal, along with an adhesive layer of TiO_2. Gold shows poor attachment with silica. So, we have introduced the adhesive layer. TiO_2 helps gold to boost up the sensing performance by elevating the surface plasmonic excitation. Because of TiO_2 having higher RI, when it is allocated on the sensor surface, it can create better coupling between photons and polaritons. The ideal airhole parameters found after proper anatomization of the design are $da_1 = 1.27\mu m$, $da_2 = 1.20\mu m$, $da_3 = 1.65\mu m$, and $da_4 = 2.2\mu m$. The distance between two airholes is marked as pitch, Λ which is kept at $2.9\mu m$. The suitable thickness of gold and TiO_2 for both the D channel and the deep groove is kept at 80nm and 9nm, respectively. The D channel radius is $2.40\mu m$, and the U-shaped deep groove has a height of $4.83\mu m$ and a width of $1.67\mu m$. The stack and draw technique supports the formation of the square lattice airholes [20], where pulsed lasers can be utilized to form the microchannels [21]. The side polishing method is an effective way of fiber polishing [22]. Chemical vapor deposition and atomic layer deposition allows the formation of nano-metallic layers with minimized surface roughness [23]. A femtosecond laser can create microchannels in optical fibers [24]. Focused ion beaming to create deep groove milled microchannels has been reported earlier [25].

Fused silica is employed as the base material because of its low absorption loss as well as high mechanical strength. The Sellmeier's equation dictates the fused silica RI, η_{si} [26]:

$$\eta_{si}^2(\lambda) = 1 + \frac{B_1\lambda^2}{\lambda^2 - C_1} + \frac{B_2\lambda^2}{\lambda^2 - C_2} + \frac{B_3\lambda^2}{\lambda^2 - C_3} \quad (3)$$

where $B_1, B_2, B_3, C_1, C_2, C_3$ are the Sellmeier constants for silica. Numerical values of each constant are $B_1 = 0.696163$, $B_2 = 0.4079426$, $B_3 = 0.8974794$, $C_1 = 4.67914 \times 10^{-3}\mu m^2$, $C_2 = 1.3512 \times 10^{-2}\ \mu m^2$ and $C_3 = 97.934\ \mu m^2$ [5].

The RI of gold can be calculated as [10]:

$$n_{Au}^2(\lambda) = \epsilon_d = \epsilon_\infty - \frac{\omega_D^2}{\omega(\omega + j\gamma D)} - \frac{\Delta\epsilon\Omega_L^2}{(\omega^2 - \Omega_L^2) + j\Gamma_L\omega} \quad (4)$$

where $\epsilon_\infty = 5.9673$ is the permittivity of gold at a high frequency. ω_D, γ_D, Γ_L, Ω_L are the plasma frequency, damping frequency, spectral width, and oscillator strength of Lorentz oscillators, respectively. All the parameters for the above equation are taken from [10].

A thin TiO_2 layer is placed between gold and silica for strengthening the attachment of gold with silica. TiO_2 also raises the interaction between surface plasmons and its joining material, gold. The RI of titanium oxide can be expressed as [10]:

$$n_{TiO_2}^2 = 5.913 + \frac{2.441 \times 10^7}{(\lambda^2 - 0.803 \times 10^7)} \quad (5)$$

where n_{TiO_2} is the wavelength-dependent RI of TiO_2.

The whole numerical analysis has been carried out using Comsol Multiphysics as a simulation tool. The total fiber radius is kept at $12.2\mu m$ with a non-physical PML having a thickness of $1.2\mu m$. The PML acts like a boundary condition which absorbs surface radiations and reflected light at the boundary. The PML's physical and the optical properties are kept the same as the base fiber material of the sensor to avoid a significant effect on sensing performance.

An experimental setup for the sensor's practical understanding is depicted in Figure 1 (b) as a resemblance. Broadband or super-continuum light source can be utilized and passed through a polarizer. A polarizer controller can also be used to have linearly polarized light. The polarized light can enter into single-mode fiber (SMF) via the splicing technique. An analyte channel has been introduced in our sensor at the outer layer, which eases the analyte's inlet and outlet. A pump can control the inlet and outlet. SPR establishes a binding environment between the ligands of the plasmonic metal and the analyte, which gives relocation of resonance peak resulting in either a blue or redshift of the response curve. An optical spectrum analyzer (OSA) can be used to sense the wavelength shifts, and a computer can be utilized to analyze the output.

IV. SIMULATIONS AND RESULTS

A. WAVELENGTH INTERROGATION METHOD

The core and the SPP mode's field profiles are shown in Fig. 2 (a) and (b). Because of the lattice structure's precise

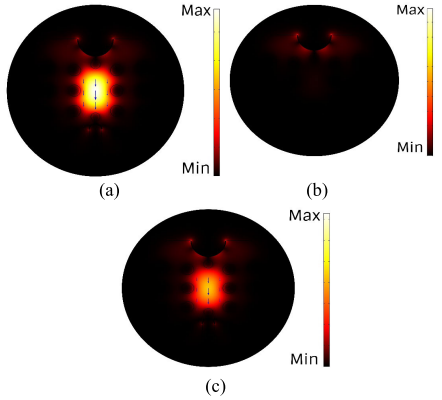

FIGURE 2. Electric field profile of the (a) core mode (b) SPP mode and (c) the resonance coupling.

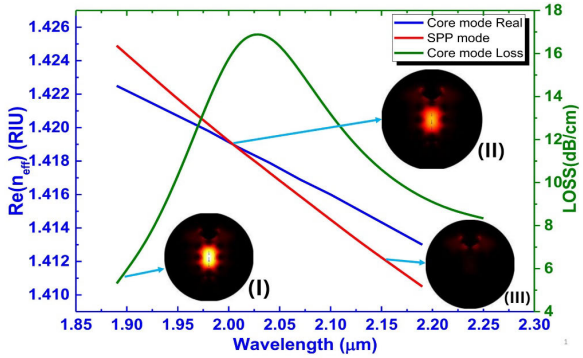

FIGURE 3. The real part of the effective index of the core mode(blue), SPP mode (red) and confinement loss of the core mode (green) with respect to wavelength alterations.

photonic crystal orientation, the incident light is guided through the core. The evanescent field of the core guided mode causes the energy leakage from the guided EM wave to the SPWs. At the phase-matching condition, the highest energy content is transferred from the core mode to the SPP mode, which is portrayed by the resonance coupling mode in Fig. 2(c). The square lattice design with increasing diameter from inwards to outwards with a D-channel and a deep groove at the bottom better interlinks the evanescent waves from the core to the polaritons. This enhances the coupling for a broad range of refractive indexes of the analytes as more analyte volume can interact with the core guiding light. The plasmonic metal introduced at the deep groove's apex lets the evanescent field interact with lesser damping. Fig. 3 shows the dispersion relations, the real part of the refractive indices of the core and the SPP mode, along with the confinement loss curve. The crossing of the real parts of both the modes dictates that incomplete coupling has taken place for the lattice design. The crossing ensures the phase matching of the EM wave with the SPW. The wavelength of the incident EM wave at the point of the crossing is the resonant wavelength. Any kind of minuscule changes in the analyte causes the optical properties of the analyte to change as well, particularly, the refractive index. Hence, the RI alteration of the analyte causes the overall effective mode index to change, which

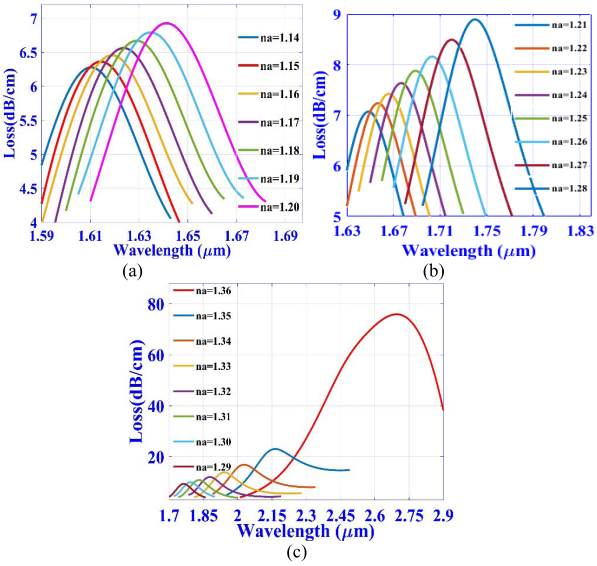

FIGURE 4. Loss curves for analyte refractive index variations (a) 1.14-1.20 (b) 1.21-1.28 and (c) 1.29-1.36.

causes the crossing to take place at different wavelengths. That is, the resonant wavelength shifts with the analyte RI alterations. From Fig. 4, it is evident that the loss curves show red shifting with the increment in the analyte RI. The probable cause for the red shifting of the resonant wavelength, λ is that higher RI of analyte on the periphery causes the damping of the plasmonic waves. This causes the propagation constants to decrease, resulting in the refractive index matching at higher wavelengths.

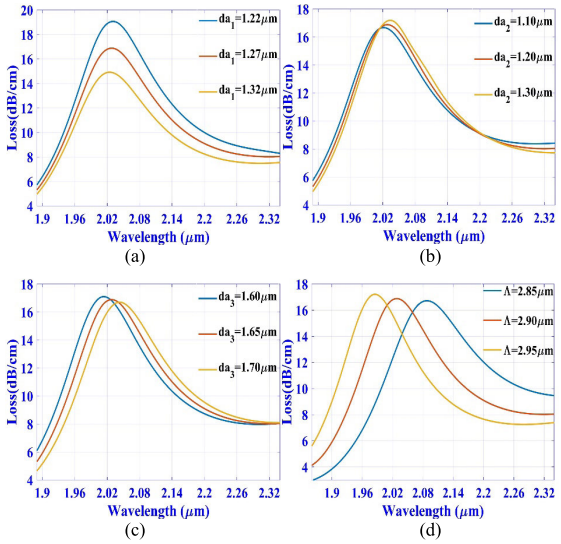

FIGURE 5. Loss curves for diameter variations (a) da_1 (b) da_2 (c) da_3 and pitch (d) variations at 1.34RI of the analyte.

The fabrication tolerance has been studied on the lattice design numerically. The airhole diameter da_1, da_2, and da_3 variations are elucidated in Fig. 5 (a), (b), (c). The tolerance of da_1 has a greater effect on the sensor response. As it directly lies in between the core and the metal-dielectric interface,

decreasing this airhole diameter causes greater energy transfer between photon and polariton, resulting in better coupling. da_2 variations have a lesser effect on the loss curves as the surface plasmons are lesser in the groove's apex. D-shaped channel diameter is kept at 4.8μm and U-shaped groove width is kept at 1.67μm in our work. From these two values, it is evident that generation of the evanescent field and the amount of surface plasmons are much higher in the D-shaped dielectric interface than that of the U-shaped groove dielectric interface because of the D-shaped channel having much higher area. da_2 airhole is placed just above the U-shaped groove, where the amount of surface plasmons and their coupling with the generated evanescent field is not high. For this reason, we have not seen any significant changes in the loss curves in Fig. 5(b) although we have varied da_2 by almost $\pm$8.35%. On the contrary, da_1 airhole is placed just under the D-shaped channel where the amount of surface plasmons and generation of evanescent field is high. Hence, we saw a significant change in loss curves in Fig. 5(a) although we varied da_1 only by $\pm$3.9%. It can be added that the presence of da_1 and da_2 comes off with great significance for confining light in the core. Without these airholes, a stable core mode cannot be obtained with respect to sweeping the wavelength of the incoming light.

The increment of da_3 causes a slight red-shifting of the curve. Pitch variations have a negligible effect on the energy transfer between the two modes, as depicted in Fig.5 (d). However, the resonant wavelength shows blue shifting with an increment in the pitch, Λ. As the gap between the airholes is increased, the confinement of light in the core decreases, which excites the surface plasmons a little lesser. The performance of the sensor corresponding to analyte RI variations has been tabulated in Table 1. According to the wavelength interrogations, the wavelength sensitivity parameter evaluates the sensing response of the sensor, which is primarily dependent on the resonance λ peak shifts. This shifting of the loss curve is peaked by a spectrometer at the output to detect the analyte changes. The wavelength sensitivity, S_λ is defined [10]

$$S_\lambda[nm/RIU] = \frac{\Delta\lambda}{\Delta n_a} \tag{6}$$

where, $\Delta\lambda$ is the peak wavelength shifts and Δn_a denotes to successive analyte RI changes. The sensor's highest S_λ for the analyte changes from 1.35-1.36RI, which is 53,800nm/RIU. The S_λ increases non-linearly from lower analyte RI to the higher ones.

For the least possible detection of spectral shifting, the sensor wavelength resolution evaluates the sensor response with respect to the analyte alterations [27]

$$R = \Delta n_a \Delta\lambda_{min}/\Delta\lambda_{peak} RIU \tag{7}$$

where, $\Delta\lambda_{min} = 0.1nm$ is considered as the minimum spectral resolution [10]. The R is inversely proportional to S_λ. The proposed sensor exhibits an R of 1.859×10^{-6} RIU.

TABLE 1. Sensor performance within sensing range.

Analyte Index	Loss Peak α(dB/cm)	λ_{peak} (μm)	Resonant Peak Shift (nm)	S_λ (nm/RIU)
1.14	6.277	1.610	4	400
1.15	6.362	1.614	5	500
1.16	6.456	1.619	4	400
1.17	6.562	1.623	6	600
1.18	6.669	1.629	6	600
1.19	6.790	1.635	7	700
1.20	6.926	1.642	7	700
1.21	7.074	1.649	8	800
1.22	7.239	1.657	9	900
1.23	7.425	1.666	11	1100
1.24	7.637	1.677	12	1200
1.25	7.880	1.689	14	1400
1.26	8.161	1.703	17	1700
1.27	8.494	1.720	20	2000
1.28	8.896	1.740	24	2400
1.29	9.393	1.764	30	3000
1.30	10.030	1.794	37	3700
1.31	10.890	1.831	47	4700
1.32	12.080	1.878	63	6300
1.33	13.880	1.941	86	8600
1.34	16.880	2.027	136	13,600
1.35	23.06	2.163	538	53,800
1.36	75.92	2.701	N/A	N/A

Fig. 6 (a) and (b) show the effect of metal layer variations on the sensor response's loss curves. An increase in the gold layer dimensions causes the coupling to decrease by a small amount. Also, the resonant λ is blue-shifted as the propagation constant of the plasmonic wave increases due to greater plasmonic oscillations. The increment of the titanium oxide layer enhances the coupling, followed by red-shifting. This will keep on increasing with the TiO_2 layer thickness. A very high thickness will cause high losses, which limit the sensing length, causing fabrication impediments. Hence, we prefer an ideal thickness of around 9nm. Fig. 6(c) and (d) portray the loss curve shifting for the analyte RI change from 1.33 to 1.34 RI. The two figures reveal the S_λ = 8200nm/RIU and S_λ = 8600nm/RIU without using TiO_2 and with using TiO_2 along with gold respectively. That is, usage of TiO_2 ameliorates the sensitivity. In addition to this, the detection accuracy increases for using TiO_2 as the Figure of Merit (FOM) is improved. This occurs for the reduction of the Full Width Half Maximum (FWHM) of the Gaussian loss curves as the two quantities are reciprocal to each other.

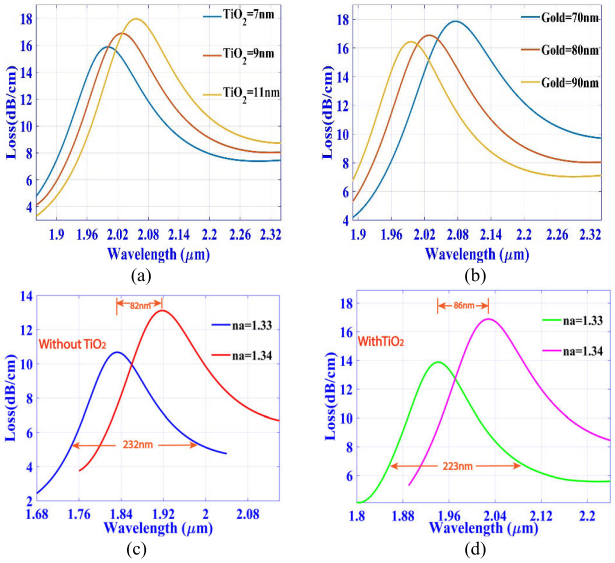

FIGURE 6. Loss curves for metal layer thickness variations at analyte index 1.34RI for (a) TiO_2 (b) gold (c) loss curve shifting for the analyte index alteration from 1.33 to 1.34RI, without TiO_2 and (d) loss curve shifting for the analyte index alteration from 1.33 to 1.34RI, with TiO_2.

The same is true for the whole sensing range of the sensor. TiO_2 is significant as an adhesive layer for gold attachment on silica. It is important that this additional adhesive layer does not intervene with the sensing potential of the sensor. The didactic inference from Fig. 6(c) and (d) suggests that TiO_2 further enhances the sensitivity instead of impeding it. Hence, we promote the usage of this adhesive layer along with the plasmonic metal.

B. AMPLITUDE INTERROGATION METHOD

Amplitude sensitivity, S_A is another significant cost-effective means of judging the sensor performance. An OSA measures the resonant wavelength shifts. However, the output light intensity measured at different input EM wavelengths varies with the analyte RI alterations. The output intensity shows dips with the subsequent rise in the confinement loss. This output intensity is measured by a photodetector, which is a cheap means of getting viable output for detecting analytes. Good S_A readings of any sensor pave the way for the sensor to be used with a photodetector to get good transmittance curve dips at the resonant λ. Fig. 7 (a) and (b) show the S_A shifts with RI variations. Increasing the analyte RI causes the S_A curves to be red-shifted with a non-linear rise in the sensitivity. The S_A is stated as [28]

$$S_A(\lambda)\left[RIU^{-1}\right] = -\frac{1}{\alpha(\lambda, n_a)}\frac{\delta\alpha(\lambda, n_a)}{\delta n_a} \tag{8}$$

where, $\alpha(\lambda, n_a)$ is the confinement loss for any analyte RI, δn_a is the successive analyte RI difference and $\delta\alpha(\lambda, n_a)$ is the difference of the loss obtained for consecutive analyte RI. The highest S_A of the sensor is found to be 328 RIU^{-1}.

The effect of metal layer thickness variations has been studied on the S_A and depicted in Fig. 8 (a) and (b).

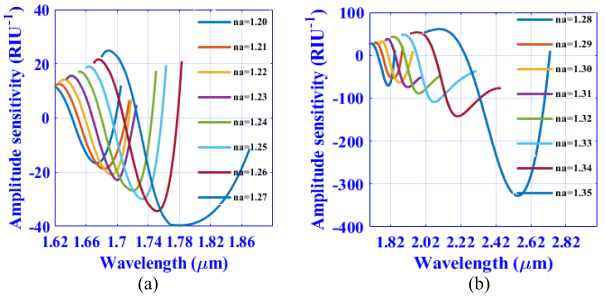

FIGURE 7. Amplitude Sensitivity curves for analyte index sensing range (a) 1.20-1.27 RI and (b) 1.28-1.35 RI.

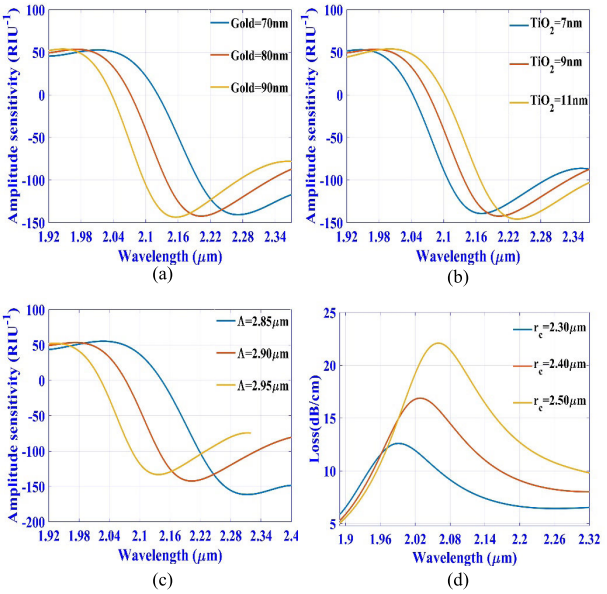

FIGURE 8. Amplitude Sensitivity curves with respect to (a) gold layer thickness variations (b) TiO_2 layer thickness variations, (c) pitch variations and (d) channel variations on the loss curve.

The increment of the gold layer, and the TiO_2 layer causes the resonance λ to shift, causing the amplitude sensitivity curves to shift. Increasing the gold layer causes the blue shifting of the amplitude sensitivity curve and increasing the TiO_2 layer causes red-shifting. As mentioned earlier, an increment of the pitch results in the blue shifting of the resonance λ. This results in the blue shifting of the S_A curve as shown in Fig. 8(c).

Fig. 8(d) elucidates the effects of the channel area variations on the sensor response. It is evident that, with the increase of channel radius the loss increases, followed by slight redshifts. As the channel area increases, more analyte volume can interact with more surface plasmons on the metal. This causes more energy transfer at the resonance conditions.

C. COMPARATIVE DISCUSSION

Table 2 comes forward with a relativistic study of the proposed sensor with respect to the other proposed designs in terms of the S_λ and the analyte RI sensing range. All the other

TABLE 2. Comparison of the sensor performance with other recent publications.

Ref.	Structure	WS (S_λ) (nm/RIU)	RI Sensing Range
[10]	Hexagonal lattice	28,000	1.33-1.42
[17]	Circular slotted D-channel	16,000	1.40-1.46
[29]	Concave shaped	9314.28	1.33-1.38
[30]	Spiral lattice	23,000	1.32-1.40
[31]	H-shaped	25,900	1.33-1.49
[32]	Square lattice	25,000	1.33-1.38
[13]	Two-sided open channel	5,000	1.33-1.39
[33]	Hollow core	21,000	1.33-1.42
[34]	Series-wound	17,500	1.13-1.35
[12]	D-shaped	20,000	1.18-1.36
[35]	Concave shaped	10,700	1.19-1.29
[36]	D-shape	15,000	1.22-1.33
[9]	Square lattice	40,000	1.33-1.53
Proposed design	D-channel deep groove	53,800	1.14-1.36

references are proposed designs of PCF SPR sensors, based on FEM, whose results have been numerically investigated. Our proposed lattice design has been able to gain a very high sensitivity in terms of wavelength interrogations for a very wide analyte sensing range. The wide analyte sensing range includes any liquid analyte having a refractive index range of 1.14-1.36 RI. References [12], [34]–[36] illustrate sensor works targeted for low analyte RI detections. However, with our non-linear rise of wavelength sensitivity, the sensing readings are much higher in a broader sensing range of analytes. A higher maximum sensitivity leads to rising slopes when going from any low RI analyte to the higher one. This indicates the improvement of the average sensitivity of the sensor for the whole sensing range. The comparative analysis with the other published lattice design works shows different lattice shapes with various photonic crystal arrangements. However, such types of proposed models lack the precise arrangement for the guided photons to couple with the polaritons for a broad sensing range, such that the sensitivity to the analyte RI alteration is high enough within the working range. The milled channel introduced with the open D-channel and the enhanced form of the well-calibrated photonic crystal lattice design have produced the desired results that have been necessary for the domain of PCF-SPR sensor works.

D. SENSOR EVALUATION

The sensor shows a non-linear rise in the resonant wavelength loss values for the increment of the incident wavelength. This has been shown in Fig. 9(a). Fig. 9(b) portrays the sensing length of the sensor with respect to the analyte index alterations.

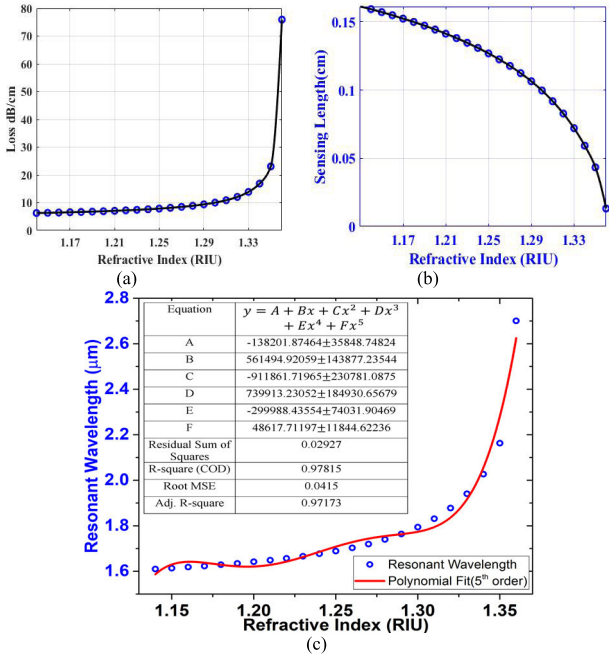

FIGURE 9. Response of the sensor for analyte RI alterations in terms of (a) confinement loss at resonant λ (b) sensing length of the sensor and (c) resonant λ.

The actual sensing length for such sensors has a reciprocal relationship with the confinement loss at the resonant λ [32].

$$L = \frac{1}{\alpha(\lambda, n_a)} \tag{9}$$

Greater confinement loss impedes the practical realization of the sensor as it decreases its sensing length. This makes it harder for the practical analysis of the sensor when splicing with fibers at the input and the output. The proposed sensor shows a maximum CL = 75.92 dB/cm, which is reasonably low in comparison to the other sensor works previously done. The sensor shows a non-linear rise in the resonant λ with increasing RI of analytes. A polynomial is fitted to the 5th order for the resonant λ increment with the analyte alterations in the increasing order, as illustrated in Fig. 9(c). This gives the characteristic polynomial equation for the sensing performance. Polynomial fitting accuracy largely depends on two factors; 1. Adjusted R^2 value and 2. Root mean square error (Root MSE). A polynomial fit is considered to be the most accurate when the adjusted R^2 value is close to 1 and the Root MSE is close to 0. A 5th order polynomial fit gives the most accurate fitting in terms of these two factors. It has been also highlighted in Fig. 9(c).

A better Figure of merit (FOM) can improve the sensor response in terms of realizing the output response from the

unwanted noise signals. The FOM is reciprocal to the full width of the half maximum (FWHM) of the gaussian sensor response [10].

$$FOM = \frac{S_\lambda}{FWHM} \tag{10}$$

The highest figure of merit for the sensor design is 105 RIU^{-1}. The figure of merit improves for the increase in wavelength sensitivity at higher analyte RI. However, the FWHM consequently decreases with analyte RI increments.

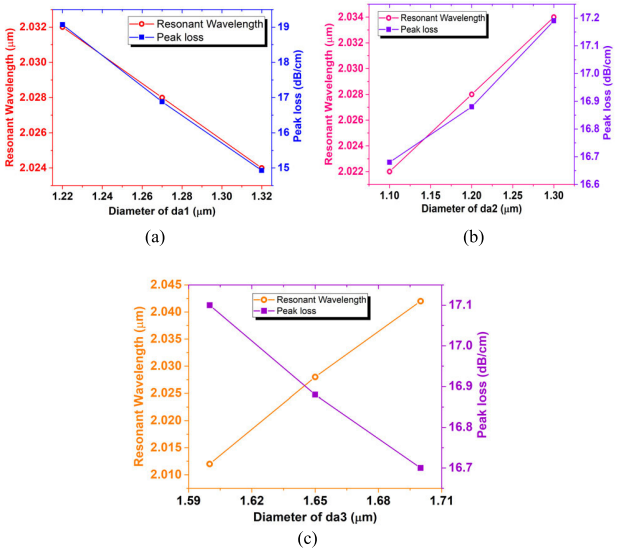

FIGURE 10. Resonant wavelength and corresponding loss as a function of (a) da_1, (b) da_2 and (c) da_3.

The study of the optical physics behind the loss curve shifts in Fig. 5 and 6, as mentioned earlier, can directly lead to Fig. 11 and 12. Fig. 10(a) reveals that the sensor shows almost a linear response with equal negative slopes for the resonant λ and the corresponding loss for increasing the diameter da_1. The same goes for da_2 with rising slope, depicted in Fig. 10(b). Fig. 10(c) shows a reciprocal relationship between resonant λ and loss for da_3. Fig. 11(a) focuses the same for the gold layer thickness increments. Increasing gold film thickness results in the change of resonant λ and loss with negative slope. TiO_2 thickness changes them with positive slopes, the slope of resonant λ being a bit higher, as shown in Fig. 11(b). Fig. 11 (c) illustrates that there exists almost a reciprocal relationship between the two variables under study for pitch variations. Fig. 11(d) elucidates the changes on them having almost equal positive slopes for the increasing D-channel radius. These relationships give an intuitive idea of the sensor response with respect to the parameters under study, revealing more about the fabrication tolerance.

V. ANECDOTE FOR FUTURE IMPROVEMENTS

As inferred previously, the quality simulation works and their numerical investigations give a broad spectrum of data and knowledge about how to go about with the geometrical features, such that the experimental researchers can correlate more about the geometry of the design and the

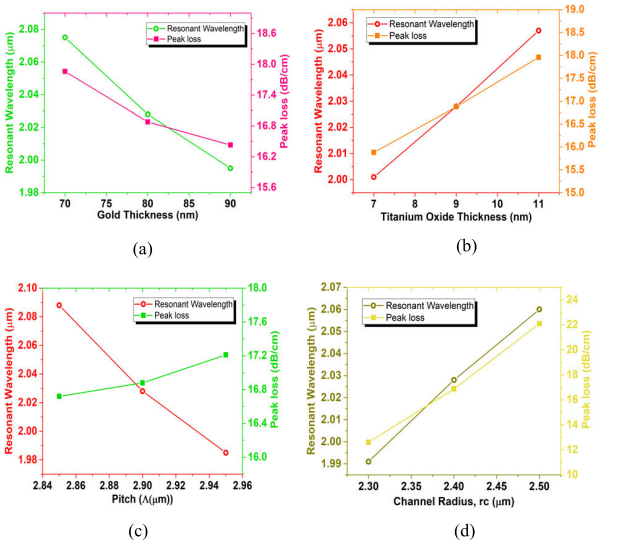

FIGURE 11. Resonant wavelength and corresponding loss as a function of (a) gold thickness, (b) TiO_2 thickness, (c) pitch and (d) channel radius.

sensor response. With a view to achieving that, wavelength sensitivity and the amplitude sensitivity have been extensively studied. Lower birefringence peak shift study is another way to go about judging the sensor response [27]. However, the sensitivity enhancement factor (SEF) comes forward from a pragmatic point of view in judging the sensor response [37]. It gives a better estimation of the content of the target molecules required for obtaining a detectable signal by selective localization in the strong fields. Besides, in surface enhanced Raman scattering sensors, substrates with high SEFs are desired [38]. Analysis of a PCF SPR sensor in terms of SEF has not been yet carried out. But it is matter of concern to study in our future works.

VI. CONCLUSION

In this work, a milled deep groove has been introduced into the fiber sensor design with an open D-channel. This results in more volume of the analyte to interact with the core mode. This broadens the analyte sensing capability of the sensor, ranging from 1.14-1.36 RI. The plasmonic oscillations occurring in very close proximity of the stable core mode, due to the lattice design's geometric orientations result in improved spectral sensitivity. The highest wavelength sensitivity is 53,800 nm/RIU with the highest amplitude sensitivity of 328 RIU^{-1}. High sensitivity having such a broad sensing range makes the sensor design suitable for dynamic biochemical detections.

REFERENCES

[1] M. A. Mollah, S. M. R. Islam, M. Yousufali, L. F. Abdulrazak, M. B. Hossain, and I. S. Amiri, "Plasmonic temperature sensor using D-shaped photonic crystal fiber," *Results Phys.*, vol. 16, Mar. 2020, Art. no. 102966.

[2] I. Stemmler, A. Brecht, and G. Gauglitz, "Compact surface plasmon resonance-transducers with spectral readout for biosensing applications," *Sens. Actuators B, Chem.*, vol. 54, nos. 1–2, pp. 98–105, Jan. 1999.

[3] J. Homola, "Present and future of surface plasmon resonance biosensors," *Anal. Bioanal. Chem.*, vol. 377, no. 3, pp. 528–539, Oct. 2003.
[4] T. H. Talukdar, G. D. Allen, I. Kravchenko, and J. D. Ryckman, "Single-mode porous silicon waveguide interferometers with unity confinement factors for ultra-sensitive surface adlayer sensing," *Opt. Exp.*, vol. 27, no. 16, p. 22485, 2019.
[5] M. A. Jabin, K. Ahmed, M. J. Rana, B. K. Paul, M. Islam, D. Vigneswaran, and M. S. Uddin, "Surface plasmon resonance based titanium coated biosensor for cancer cell detection," *IEEE Photon. J.*, vol. 11, no. 4, pp. 1–10, Aug. 2019.
[6] M. A. Mollah, M. Yousufali, I. M. Ankan, M. M. Rahman, H. Sarker, and K. Chakrabarti, "Twin core photonic crystal fiber refractive index sensor for early detection of blood cancer," *Sens. Bio-Sensing Res.*, vol. 29, Aug. 2020, Art. no. 100344.
[7] G. Qiu, Z. Gai, Y. Tao, J. Schmitt, G. A. Kullak-Ublick, and J. Wang, "Dual-functional plasmonic photothermal biosensors for highly accurate severe acute respiratory syndrome coronavirus 2 detection," *ACS Nano*, vol. 14, no. 5, pp. 5268–5277, May 2020.
[8] J. N. Anker, W. P. Hall, O. Lyandres, N. C. Shah, J. Zhao, and R. P. Van Duyne, "Biosensing with plasmonic nanosensors," in *Nanoscience and Technology*, vol. 557, no. 5. London, U.K.: Macmillan Publishers, 2009, pp. 308–319.
[9] K. Ahmed, M. J. Haque, M. A. Jabin, B. K. Paul, I. S. Amiri, and P. Yupapin, "Tetra-core surface plasmon resonance based biosensor for alcohol sensing," *Phys. B, Condens. Matter*, vol. 570, pp. 48–52, Oct. 2019.
[10] M. A. Mahfuz, M. A. Hossain, E. Haque, N. H. Hai, Y. Namihira, and F. Ahmed, "Dual-core photonic crystal fiber-based plasmonic RI sensor in the visible to near-IR operating band," *IEEE Sensors J.*, vol. 20, no. 14, pp. 7692–7700, Jul. 2020.
[11] X. Chen, C. Li, X. Chen, L. Xia, and C. Li, "Surface plasmon resonance sensor based on a novel D-shaped photonic crystal fiber for low refractive index detection," *IEEE Photonics J.*, vol. 10, no. 1, pp. 1–9, Jan. 2018.
[12] E. Haque, M. A. Hossain, F. Ahmed, and Y. Namihira, "Surface plasmon resonance sensor based on modified *D*-shaped photonic crystal fiber for wider range of refractive index detection," *IEEE Sensors J.*, vol. 18, no. 20, pp. 8287–8293, Oct. 2018.
[13] S. Akter, M. Z. Rahman, and S. Mahmud, "Highly sensitive open-channels based plasmonic biosensor in visible to near-infrared wavelength," *Results Phys.*, vol. 13, Jun. 2019, Art. no. 102328.
[14] M. A. Khalek, S. Chakma, K. Ahmed, B. K. Paul, D. Vigneswaran, and R. Zakaria, "Materials effect in sensing performance based on surface plasmon resonance using photonic crystal fiber," *Plasmonics*, vol. 14, no. 4, pp. 861–867, Aug. 2019.
[15] C. Liu, L. Yang, X. Lu, Q. Liu, F. Wang, J. Lv, T. Sun, H. Mu, and P. K. Chu, "Mid-infrared surface plasmon resonance sensor based on photonic crystal fibers," *Opt. Exp.*, vol. 25, no. 13, pp. 14227–14237, 2017.
[16] C. Liu, J. Wang, X. Jin, F. Wang, L. Yang, J. Lv, G. Fu, X. Li, Q. Liu, T. Sun, and P. K. Chu, "Near-infrared surface plasmon resonance sensor based on photonic crystal fiber with big open rings," *Optik*, vol. 207, Apr. 2020, Art. no. 164466.
[17] M. N. Sakib, S. M. R. Islam, T. V. Mahendiran, L. F. Abdulrazak, M. S. Islam, I. M. Mehedi, Q. M. Kamrunnahar, M. Momtaj, M. W. Hassan, I. S. Amiri, and M. B. Hossain, "Numerical study of circularly slotted highly sensitive plasmonic biosensor: A novel approach," *Results Phys.*, vol. 17, Jun. 2020, Art. no. 103130.
[18] T. Wu, Y. Shao, Y. Wang, S. Cao, W. Cao, F. Zhang, C. Liao, J. He, Y. Huang, M. Hou, and Y. Wang, "Surface plasmon resonance biosensor based on gold-coated side-polished hexagonal structure photonic crystal fiber," *Opt. Exp.*, vol. 25, no. 17, p. 20313, 2017.
[19] M. F. O. Hameed and S. Obayya, Eds., *Computational Photonic Sensors*. Cham, Switzerland: Springer, 2019.
[20] D. Pysz, I. Kujawa, R. Stępień, M. Klimczak, A. Filipkowski, M. Franczyk, L. Kociszewski, J. Buźniak, K. Haraśny, and R. Buczyński, "Stack and draw fabrication of soft glass microstructured fiber optics," *Bull. Polish Acad. Sci. Tech. Sci.*, vol. 62, no. 4, pp. 667–682, Dec. 2014.
[21] E. Haque, M. Anwar Hossain, Y. Namihira, and F. Ahmed, "Microchannel-based plasmonic refractive index sensor for low refractive index detection," *Appl. Opt.*, vol. 58, no. 6, p. 1547, 2019.
[22] A. A. Rifat, R. Ahmed, G. A. Mahdiraji, and F. R. M. Adikan, "Highly sensitive D-shaped photonic crystal fiber-based plasmonic biosensor in visible to near-IR," *IEEE Sensors J.*, vol. 17, no. 9, pp. 2776–2783, May 2017.
[23] M. A. Mahfuz, M. R. Hasan, M. R. Momota, A. Masud, and S. Akter, "Asymmetrical photonic crystal fiber based plasmonic sensor using the lower birefringence peak method," *OSA Continuum*, vol. 2, no. 5, p. 1713, 2019.
[24] A. van Brakel, C. Grivas, M. N. Petrovich, and D. J. Richardson, "Micro-channels machined in microstructured optical fibers by femtosecond laser," *Opt. Exp.*, vol. 15, no. 14, p. 8731, 2007.
[25] F. Wang, W. Yuan, O. Hansen, and O. Bang, "Selective filling of photonic crystal fibers using focused ion beam milled microchannels," *Opt. Exp.*, vol. 19, no. 18, p. 17585, 2011.
[26] H. Talukder, M. I. A. Isti, S. Nuzhat, and S. K. Biswas, "Ultra-high negative dispersion based single mode highly nonlinear bored core photonic crystal fiber (HNL-BCPCF): Design and numerical analysis," *Brazilian J. Phys.*, vol. 50, no. 3, pp. 263–271, Jun. 2020.
[27] M. I. A. Isti, H. Talukder, S. M. R. Islam, S. Nuzhat, A. S. M. S. Hosen, G. H. Cho, and S. K. Biswas, "Asymmetrical D-channel photonic crystal fiber-based plasmonic sensor using the wavelength interrogation and lower birefringence peak method," *Results Phys.*, vol. 19, Dec. 2020, Art. no. 103372.
[28] A. Shafkat, "Analysis of a gold coated plasmonic sensor based on a duplex core photonic crystal fiber," *Sens. Bio-Sens. Res.*, vol. 28, Jun. 2020, Art. no. 100324.
[29] A. K. Pathak and V. K. Singh, "SPR based optical fiber refractive index sensor using silver nanowire assisted CSMFC," *IEEE Photon. Technol. Lett.*, vol. 32, no. 8, pp. 465–468, Apr. 15, 2020.
[30] M. A. Mahfuz, M. A. Hossain, E. Haque, N. H. Hai, Y. Namihira, and F. Ahmed, "A bimetallic-coated, low propagation loss, photonic crystal fiber based plasmonic refractive index sensor," *Sensors*, vol. 19, no. 17, p. 3794, Sep. 2019.
[31] H. Han, D. Hou, L. Zhao, N. Luan, L. Song, Z. Liu, Y. Lian, J. Liu, and Y. Hu, "A large detection-range plasmonic sensor based on an H-shaped photonic crystal fiber," *Sensors*, vol. 20, no. 4, p. 1009, Feb. 2020.
[32] M. S. Islam, C. M. Cordeiro, J. Sultana, R. A. Aoni, S. Feng, R. Ahmed, M. Dorraki, A. Dinovitser, B. W.-H. Ng, and D. Abbott, "A Hi-Bi ultra-sensitive surface plasmon resonance fiber sensor," *IEEE Access*, vol. 7, pp. 79085–79094, 2019.
[33] M. B. Hossain, S. M. R. Islam, K. M. T. Hossain, L. F. Abdulrazak, M. N. Sakib, and I. S. Amiri, "High sensitivity hollow core circular shaped PCF surface plasmonic biosensor employing silver coat: A numerical design and analysis with external sensing approach," *Results Phys.*, vol. 16, Mar. 2020, Art. no. 102909.
[34] J. Wang, C. Liu, F. Wang, W. Su, L. Yang, J. Lv, G. Fu, X. Li, Q. Liu, T. Sun, and P. K. Chu, "Surface plasmon resonance sensor based on coupling effects of dual photonic crystal fibers for low refractive indexes detection," *Results Phys.*, vol. 18, Sep. 2020, Art. no. 103240.
[35] Z. Yang, L. Xia, C. Li, X. Chen, and D. Liu, "A surface plasmon resonance sensor based on concave-shaped photonic crystal fiber for low refractive index detection," *Opt. Commun.*, vol. 430, pp. 195–203, Jan. 2019.
[36] C. Liu, J. Wang, F. Wang, W. Su, L. Yang, J. Lv, G. Fu, X. Li, Q. Liu, T. Sun, and P. K. Chu, "Surface plasmon resonance (SPR) infrared sensor based on D-shape photonic crystal fibers with ITO coatings," *Opt. Commun.*, vol. 464, Jun. 2020, Art. no. 125496.
[37] M. Sarkar, M. Chamtouri, J. Moreau, M. Besbes, and M. Canva, "Introducing 2D confined propagating plasmons for surface plasmon resonance sensing using arrays of metallic ribbons," *Sens. Actuators B, Chem.*, vol. 191, pp. 115–121, Feb. 2014.
[38] M. Li, S. K. Cushing, and N. Wu, "Plasmon-enhanced optical sensors: A review," *Analyst*, vol. 140, no. 2, pp. 386–406, 2015.

M. HUSSAYEEN KHAN ANIK is currently pursuing the B.Sc. degree in education from the Faculty of Electrical and Electronic Engineering, Shahjalal University of Science and Technology. He is undergoing through a research program in photonics and plasmonics at his respective institution. His research interests include fiber optics, photonics, plasmonics, and optical biosensors.

M. IFAZ AHMAD ISTI received the B.Sc. degree in electrical and electronic engineering from the Shahjalal University of Science and Technology, Sylhet, Bangladesh, in 2020. He is a former secretary of IEEE, Student Branch, SUST. He is currently working as a Research Assistant with the Department of Electrical Engineering, Shahjalal University of Science and Technology, in the field of optics and photonics. His research interests include fiber optics, photonic crystals, plasmonics, and optical biosensors.

S. M. RIAZUL ISLAM (Member, IEEE) received the Ph.D. degree in information and communication engineering from Inha University, South Korea, in 2012. He has been working as a Professor with the Department of Computer Science and Engineering, Sejong University, South Korea, since March 2017. He is a Distinguished Professor with the Chongqing College of Electronic Engineering, China. From 2014 to 2017, he worked at the Wireless Communications Research Center, Inha University, South Korea, as a Postdoctoral Fellow. From 2016 to 2017, he was also affiliated with Memorial University, Canada, as a non-resident Postdoctoral Fellow. From 2005 to 2014, he was with the University of Dhaka, Bangladesh, as an Assistant Professor and a Lecturer with the Department of Electrical and Electronic Engineering. In 2014, he worked at the Department of Solution Lab, Samsung Research and Development Institute Bangladesh (SRBD), as a Chief Engineer. His research interests include wireless communications, Internet of Things, and applied machine learning.

SAKIB MAHMUD is currently pursuing the B.Sc. degree with the Department of Electrical and Electronic Engineering, Shahjalal University of Science and Technology (SUST). He is currently undertaking a research program regarding photonics and plasmonics at his respective institution. He is a member of the Institute of Electrical and Electronic Engineers (IEEE) and is currently occupying the 'Treasurer' post of the IEEE SUST Student Branch. His research interests include fiber optics, photonic crystal fiber, plasmonics, and optical biosensors.

HRITESHWAR TALUKDER (Member, IEEE) received the B.Sc. (Engg.) degree in electrical and electronic engineering from the Shahjalal University of Science and Technology, Bangladesh, in 2017, where he joined as a Lecturer. His research interests include nonlinear optics, nanophotonics, plasmonics, optical biosensor, photonic crystal fiber, and optical fiber communication.

MD. JALIL PIRAN (Member, IEEE) is currently pursuing the Ph.D. degree in electronics and radio engineering from Kyung Hee University, South Korea, in 2016. He is an Assistant Professor with the Department of Computer Science and Engineering, Sejong University, Seoul, South Korea. Subsequently, he continued his work as a Postdoctoral Research Fellow in the field of "Resource Management" and "Quality of Experience" in "5G Cellular Networks" and "Internet of Things" in the Networking Lab, Kyung Hee University. He published substantial number of technical papers in well-known international journals and conferences in research fields of "5G and 6G wireless communications, Internet of Things (IoT), multimedia communication, cognitive radio networks, applied machine learning, security, and smart grid." He received "IAAM Scientist Medal of the year 2017" for notable and outstanding research in the field of new age technology and innovation, Stockholm, Sweden. Moreover, he has been recognized as the "Outstanding Emerging Researcher" by the Iranian Ministry of Science, Technology, and Research in 2017. In addition, his Ph.D. dissertation has been selected as the "Dissertation of the Year 2016" by the Iranian Academic Center for Education, Culture, and Research in the field of electrical and communications engineering. In the worldwide communities, he is an active member of Institute of Electrical and Electronics Engineering (IEEE), since 2010, an active delegate from South Korea in Moving Picture Experts Group (MPEG), since 2013, and an active member of International Association of Advanced Materials (IAAM), since 2017.

SHOVASIS KUMAR BISWAS (Member, IEEE) received the B.Sc. and M.Sc. degrees in applied physics, electronics and communication engineering from the University of Dhaka, Dhaka, Bangladesh, in 2011 and 2013, respectively, and the M.A.Sc. degree in electrical and computer engineering from McMaster University, Canada, in 2016. He is presently working as a Lecturer with the Department of Electrical and Electronic Engineering, Independent University, Bangladesh, Dhaka, Bangladesh. He has published several papers in journals as well as in the proceedings of IEEE flagship/portfolio conferences. His research interests are nanophotonics, plasmonics, optical biosensor, photonic crystal fiber, and optical fiber communication. He is a member of the Institute of Electrical and Electronic Engineers.

KYUNG-SUP KWAK (Life Senior, IEEE) received the B.S. degree from Inha University, Inchon, South Korea, in 1977, the M.S. degree from the University of Southern California, in 1981, and the Ph.D. degree from the University of California at San Diego, in 1988, under the Inha University Fellowship and the Korea Electric Association Abroad Scholarship Grants, respectively. He worked for Hughes Network System, San Diego, CA, USA, and the IBM Network Research Center, Research Triangle Park, NC, USA, from 1988 to 1990. Since 1990, he has been with Inha University as the Inha Fellow Professor. He is currently the Inha Hanlim Professor and also the Director of the UWB Wireless Communications Research Center, South Korea. His research interests include multiple access communication systems, mobile communication systems, UWB radio systems, ad-hoc networks, and the high-performance wireless Internet. He is a member of IEICE, KICS, and KIEE.